



HAL
open science

Numerical study of ElectroAeroDynamic force and current resulting from ionic wind in emitter/collector systems

Christian Coseru, David Fabre, Franck Plouraboué

► **To cite this version:**

Christian Coseru, David Fabre, Franck Plouraboué. Numerical study of ElectroAeroDynamic force and current resulting from ionic wind in emitter/collector systems. *Journal of Applied Physics*, 2021, 129 (10), pp.103304. 10.1063/5.0041061 . hal-03179060

HAL Id: hal-03179060

<https://hal.science/hal-03179060>

Submitted on 24 Mar 2021

HAL is a multi-disciplinary open access archive for the deposit and dissemination of scientific research documents, whether they are published or not. The documents may come from teaching and research institutions in France or abroad, or from public or private research centers.

L'archive ouverte pluridisciplinaire **HAL**, est destinée au dépôt et à la diffusion de documents scientifiques de niveau recherche, publiés ou non, émanant des établissements d'enseignement et de recherche français ou étrangers, des laboratoires publics ou privés.



Open Archive Toulouse Archive Ouverte




OATAO is an open access repository that collects the work of Toulouse researchers and makes it freely available over the web where possible

This is an author's version published in: <https://oatao.univ-toulouse.fr/27560>

Official URL:

<https://doi.org/10.1063/5.0041061>

To cite this version:

Coseru, Christian  and Fabre, David  and Plouraboué, Franck  *Numerical study of ElectroAeroDynamic force and current resulting from ionic wind in emitter/collector systems.* (2021) *Journal of Applied Physics*, 129 (10). 103304. ISSN 0021-8979.

Any correspondence concerning this service should be sent to the repository administrator: tech-oatao@listes-diff.inp-toulouse.fr

Numerical study of ElectroAeroDynamic force and current resulting from ionic wind in emitter/collector systems

S. Coseru, D. Fabre, F. Plouraboué

Institut de Mécanique des Fluides de Toulouse, IMFT, Université de Toulouse, CNRS, 31400 Toulouse, France

E-mail: fpLOURAB@imft.fr

August 2020

Abstract. ElectroAeroDynamic (EAD) propulsion has recently shown a growing interest with distinct propulsive capabilities and specific advantages. These experimental observations are therefore driving interest for numerical predictions of their propulsive capabilities. Keeping with a drift region description associated with Kaptsov approximation of the corona discharge region effect, we evaluate the detailed contributions of EAD forces from electro-drift effects computation only. We propose a new regularization procedure for the numerical formulation of the electro-drift problem, allowing the convergence of the resulting iterative procedure (here a Newton method) over very large domains, using iterative adapted meshes in high gradient regions. Our predictions show a good comparison with many experimental configurations, both for the current/intensity and the propulsive force. In some cases, we identify the air drag and the Kaptsov approximation to explain discrepancies with experimental measurements. Finally, we confirm optimal configurations for staggered emitters and collectors arrays, consistently with previously reported experimental results.

Keywords: ionic wind, ElectroAeroDynamic, ElectroHydroDynamic, electric propulsion, drift region, solid propulsion aeroplane, finite element, numerical simulations, ion mobility Submitted to: *J. Phys. D: Appl. Phys.*

1. Introduction

Ionic wind generation leading to Aero-Electro-Dynamic (AED) propulsion has regain interest in the recent years from various experimental observations [1, 2, 3, 4, 5, 6, 7, 8, 9] demonstrating distinct propulsive capabilities. Indeed, AED propulsion display a much better Thrust to Power ratio than thermal engines [2, 5], by a factor 5 to 10 (from 10 to 20 N/kW , as compared to 2 N/kW for jet propulsion). Albeit limited by poor thrust density and efficiency [10, 11, 12, 2], it has the very specific advantage of being almost silent and environmental friendly. The recent first autonomous ionic wind flight of a five-meter wingspan drone [13] has opened new applicative prospects. Furthermore, it has been shown that Ionic wind propulsion is able to sustain the stationary flight of gliders such as Solar-Impulse II [7]. Hence, further

investigations of AED propulsion systems for various applications are necessary. The interest of numerical modeling in this new aerodynamic propulsion domain results from its capability of exploring many geometries so as to guide and improve better propulsive performances. Furthermore, in order to design the best architectures for these new propulsive systems, there is a need for reliable numerical predictions [14, 15, 16, 17, 18, 19, 9]. Previous numerical studies were most often performed with commercial codes [14, 15, 16, 18, 19, 9]. Nevertheless, the number of numerical studies and their cross validation with experiments are scarce in the area because of various difficulties : finite size effects, influence of poorly defined boundary conditions, convergence difficulties in large domains, modeling issues associated with various phenomena such as corona discharge, turbulence modeling,... Few numerical predictions have been compared with experimental measurements in the very same configurations, as in [?, 9], in order to assess and analyse the modeling predictability and limitations. The purpose of this contribution is to provide such comparison in various emitter/collector configurations, so as to demonstrate how much a drift-region numerical modeling of AED can be predictive of propulsive effects.

The paper is organized as follow. In section 2.1 we detail the theoretical formulation, the dimensionless version of which, given in 2.2 leads to variational formulation described in 2.3. A new regularization of the problem is given in 2.4 whilst its numerical implementation, test and validation is detailed in section 3. Section 4 provides a detailed comparison of our predictions with several experimental configurations of the literature for single emitter/single collector in 4.2, single emitter/two collectors in 4.3, two emitters/two collectors in 4.4 and finally arrays of emitters and collectors in 4.5.

2. Method

2.1. Theoretical formulation

2.1.1. *Constitutive equations and boundary conditions* The governing equations adopted here are the Poisson problem for the electric potential φ [$V \cdot m$],

$$\Delta\varphi = -\frac{\rho}{\varepsilon_0}, \quad (1)$$

ε_0 being the dielectric permittivity of free space. Charge density ρ [C/m^3] conservation (positive charges are considered here for a positive corona discharge),

$$\nabla \cdot (-\mu\rho\nabla\varphi - D_\rho\nabla\rho) = 0, \quad (2)$$

with μ the charge mobility [$m^2/V \cdot s$] and D_ρ [m^2/s], the charge diffusivity. These equations will be solved in a numerical two-dimensional (2D) domain Ω .

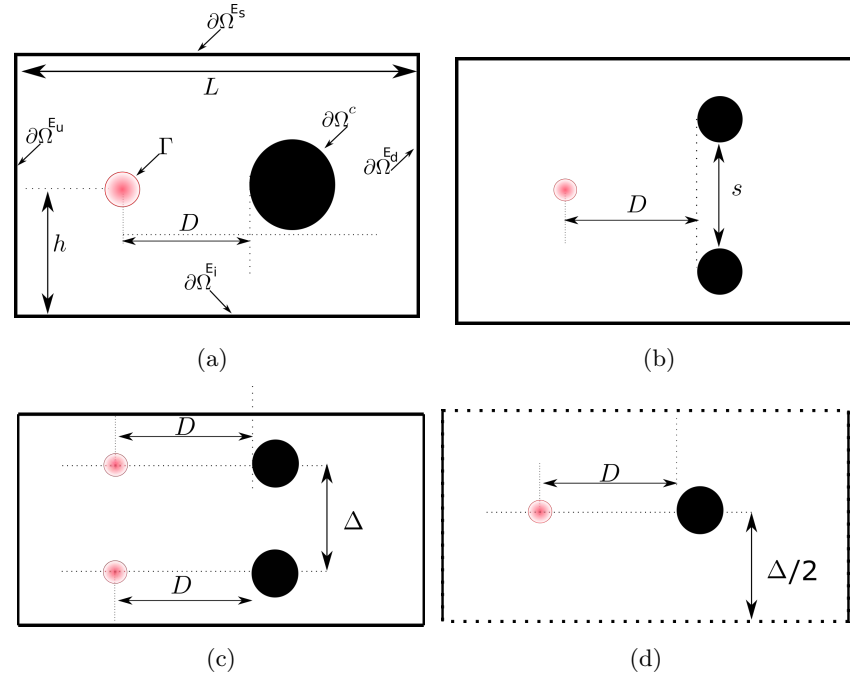


Figure 1: Sketch of the various configurations studied in this paper: (a) one emitter/one collector (1E/1C) configuration with domain boundaries and notations. (b) 1E/2C configuration where s denotes the spacing between the collectors. (c) 2E/2C with finite domain having Neumann lateral boundary conditions (d). nE/nC periodic configurations (dotted lines stands for periodic Boundary conditions). Note that D denotes the minimum longitudinal distance between emitters and collector (and not the centre-to-centre distance). The emitter with radius r_e is represented with a tiny red spot with shade area around it to depict the glow discharge region, the boundary of which is denoted Γ . The collectors are the black circles with radius R_{col} .

As in many other contributions, [20, 21, 18, 9] we omit the description of the corona discharge, and only use effective boundary conditions applied at a circle Γ corresponding to the outer bound of the corona discharge region. Noting V the tension applied between the electrodes, we will consider the following boundary conditions at surface Γ for emitter and surface $\partial\Omega^c$ for collector:

$$\varphi|_{\Gamma} = V \quad (3)$$

$$\varphi|_{\partial\Omega^c} = 0. \quad (4)$$

For every other external boundaries $\partial\Omega^E \equiv \partial\Omega^{E_u} \cup \partial\Omega^{E_s} \cup \partial\Omega^{E_d} \cup \partial\Omega^{E_i}$ (where index u, s, d, i stands for upstream, superior, downstream, inferior) we will consider two classes of boundary conditions (i) zero electric field imposed and absence of charges leaks at lateral boundaries :

$$\nabla\varphi \cdot \mathbf{n}|_{\partial\Omega^E} = 0 \quad (5)$$

$$\nabla n \cdot \mathbf{n}|_{\partial\Omega^E} = 0 \quad (6)$$

or, (ii) periodic boundary conditions pairing $\partial\Omega^{E_s}$ & $\partial\Omega^{E_i}$ in the case we consider a

periodic set of emitters and collectors together with boundary conditions (5) & (6) for $\partial\Omega^{E_a} \cup \partial\Omega^{E_d}$.

2.1.2. Kaptzov approximation A standard approximation used in the field (e.g [22, 20, 18, 9]) is to consider that an imposed electric field independent of the applied potential difference holds nearby the emitter. This Kaptzov hypothesis has been recently theoretically justified and asymptotically holds for axi-symmetrical configuration [23]. For non axi-symmetric situations it is an approximation and some improved boundary conditions have been proposed in some cases [24, 25]. More complex description of the corona discharge physics are possible (e.g [26]) but very difficult to handle in complex electrode configurations. Peek [27] law is used for a cylindrical wire in air at atmospheric pressure

$$E_{Peek} = 3.1.m\delta \left(1 + \frac{0.308}{\sqrt{r_e\delta}} \right), \quad (7)$$

where r_e the emitter radius (in *cm*), m a parameter describing the roughness effect ($m = 1$ for a smooth wire), δ is the air density ($\delta = 1$ at atmospheric pressure and reference temperature). Alternatively we also use a more general formula derived in [23] for any gas at arbitrary pressure and temperature

$$E_a = E_{ief} \left[\mathcal{W}_0 \left(\frac{r_e\beta_{ef}}{\ln(1+\gamma^{-1})} \right) \right]^{-1}, \quad (8)$$

where \mathcal{W}_0 is the principal Lambert function, E_{ief} the ionisation electric field of the gas at the given pressure and temperature, β_{ef} the pre-factor of the Townsend ionization coefficient and γ the photo-ionization coefficient (cf. [23] for more details). Thus, in the following, we set the Kaptzov approximation at Γ

$$\nabla\varphi \cdot \mathbf{n}|_{\Gamma} = E_a \quad (9)$$

with E_a either given by (7) or (8). Since the Kaptzov condition is by essence a matching condition for the outer problem governing the plasma dynamics in the drift region and that the inner discharge region in the vicinity of the emitter is not resolved, it remains unclear if this condition should be applied directly at the boundary of the emitter $\partial\Omega^e$, or at some artificial contour Γ considered as the outer bound of the discharge region; for instance a circle of radius $r_{\Gamma} = \alpha r_0$ as sketched in figure 1a. We tried this second approach and considered several values of α , leading to minor improvement of matching with experiments in some cases, but could not find a universal value α leading to improvement in all cases. Hence, we finally decided not to introduce such an arbitrary parameter, and identified the numerical bound of the drift region Γ with the boundary of the emitter $\partial\Omega^e$.

2.1.3. Force and Intensity Most experimental studies available in the literature have reported the current intensity and propulsive thrust. We now discuss how these quantities can be deduced from the solution of the electrostatic problem.

First, the current intensity I (per unit length in the span-wise direction) is

$$I = \mu \int_{\Gamma} \rho \nabla\varphi \cdot \mathbf{n} \equiv -\mu \int_{\partial\Omega^e} \rho \nabla\varphi \cdot \mathbf{n}. \quad [I/m] \quad (10)$$

Note that the possibility to evaluate the current either at the emitter (first integral over Γ) or at the collector (second integral over $\partial\Omega^c$) provides a consistency check for our computations. In the results we found that the two expressions coincide within less than 0.5%. This means that our computations are free from charge leak over the external boundaries $\partial\Omega^E$. Note that such charge leaks exist in experiments, and some numerical studies have sometimes introduced them in their boundary conditions so as to better match with their measurements [9].

Secondly, from the action/reaction principle, the total Electro-AeroDynamic (EAD) force exerted on the gas equals the propulsive force exerted onto the device [28]. This EAD force \mathbf{F}_{EAD} (per unit length in the span-wise direction) can thus be obtained from integrating local Coulomb force $\mathbf{f}_C = \rho\mathbf{E}$ over the 2D domain:

$$\mathbf{F}_{EAD} = \int_{\Omega} \mathbf{f}_C d\Omega = - \int_{\Omega} \rho \nabla \varphi d\Omega. \quad [N/m] \quad (11)$$

As such, one can not distinguish where this propulsive force acts among the various solid parts of the aeroplane (here restrained to the emitter wire and the collector only). Such a decomposition of the propulsive force can nevertheless be obtained noting that \mathbf{f}_C corresponds to the divergence of the Maxwell stress tensor

$$\mathbf{f}_C = \nabla \cdot \boldsymbol{\sigma}^M = \nabla \cdot \varepsilon_0 \left(\mathbf{E} \times \mathbf{E} - \frac{E^2}{2} \mathbf{I} \right) \quad (12)$$

with \mathbf{I} the identity tensor. Applying the divergence theorem to (11) and using (12), we get

$$\mathbf{F}_{EAD} = \varepsilon_0 \int_{\partial\Omega} \left((\mathbf{E} \cdot \mathbf{n}) \mathbf{E} - \frac{E^2}{2} \mathbf{n} \right) dS \quad (13)$$

The domain boundary decomposes into $\partial\Omega = \partial\Omega^E \cup \partial\Omega^c \cup \Gamma$ but the contribution over $\partial\Omega^E$ cancels from the boundary conditions choice. Hence the various contributions of the propulsive force on the emitter and the collector result from the evaluation of the surface integral (13) over Γ and $\partial\Omega^c$. Again, the ability to compute the EAD thrust either from a surface integral or from a boundary integral provides a consistency check for the numerical method, and results obtained with our code using (13) and (11) always agree within less than 0.5%.

2.2. Dimensionless formulation

We use R_{col} as a the reference length scale, so that the dimensionless collector radius $\hat{R}_{col} = 1$. Apart from geometrical parameters $\hat{r}_0 = r_0/R_{col}$, $\hat{D} = D/R_{col}$, the problem involves a single dimensionless parameter which can be defined as

$$\hat{\varphi}_a = \frac{V}{R_{col} E_a} \quad (14)$$

with E_a given in section 2.1.2 by (7) or (8). We introduce nondimensional variables as follow:

$$\hat{\varphi} = \frac{\varphi}{\varphi^*}, \quad \text{with } \varphi^* = V, \quad (15)$$

$$\hat{\rho} = \frac{\rho}{\rho^*}, \quad \text{with } \rho^* = \frac{\varepsilon_0 V}{R_{col}^2}. \quad (16)$$

AED force & current

6

Dimensionless form of (1) and (2) reads

$$\hat{\Delta}\hat{\varphi} = -\hat{\rho} \quad (17)$$

$$\hat{\nabla}\left(-\hat{\rho}\hat{\nabla}\hat{\varphi} - \frac{1}{Pe}\hat{\nabla}\hat{\rho}\right) = 0 \quad (18)$$

where $\hat{\nabla}$ and $\hat{\Delta}$ are the gradient and Laplacian operators expressed in terms of the non-dimensional variables, and where the electro-convective Péclet number is defined as $Pe = \mu V R_{col} / D\rho$. In this problem $Pe \gg 1$ [29, 30, 28], so that (18) is strongly hyperbolic dominated. Dimensionless boundary conditions (3) and (4) then read

$$\hat{\varphi}|_{\Gamma} = 1 \quad (19)$$

$$\hat{\varphi}|_{\Omega^e} = 0. \quad (20)$$

For external boundary conditions, the dimensionless formulation is identical as (i) and (ii) given at the end of section 2.1.1 hence, not repeated here. The Kaptzov boundary condition leads to

$$\partial_n \hat{\varphi}|_{\Gamma} = (\hat{\varphi}_a)^{-1} \quad (21)$$

Both current and force can be computed from their dimensionless counterpart following formulas

$$I = \mu\varphi^* \rho^* R_{col} \int_{\hat{\Gamma}} \hat{\rho} \hat{\nabla} \hat{\varphi} \cdot \mathbf{n} = \mu\varphi^* \rho^* \hat{I} \quad (22)$$

$$\mathbf{F}_{EAD} = \int_{\Omega} \rho \nabla \varphi = \varphi^* \rho^* R_{col} \int_{\hat{\Omega}} \hat{\rho} \hat{\nabla} \hat{\varphi} = \varphi^* \rho^* R_{col} \hat{\mathbf{F}}_{EAD} \quad (23)$$

These expressions are useful to produce sensible quantities to compare with experiments. Furthermore, the dimensionless formulation of the surface integral (13) is

$$\mathbf{F}_{EAD} = \varepsilon_0 \frac{\varphi^{*2}}{R_{col}} \int_{\partial\hat{\Omega}} \left((\hat{\mathbf{E}} \cdot \mathbf{n}) \hat{\mathbf{E}} - \frac{\hat{E}^2}{2} \mathbf{n} \right) dS \quad (24)$$

2.3. Variational formulation

To set the problem into a variational formulation, we multiply (17) by a test function φ^\dagger and integrate over the domain Ω . We incorporate the boundary condition (4) by a penalization technique, by integrating over the boundary $\delta\Omega^C$ and multiplying by a large number $1/\varepsilon_p$. This leads to:

$$\forall \varphi^\dagger, \quad \int_{\hat{\Gamma}} \varphi^\dagger \hat{E}_a - \int_{\hat{\Omega}} \hat{\nabla} \hat{\varphi} \hat{\nabla} \varphi^\dagger + \int_{\hat{\Omega}} \hat{\rho} \varphi^\dagger + \frac{1}{\varepsilon_p} \int_{\partial\hat{\Omega}^e} \varphi^\dagger \hat{\varphi} = 0 \quad (25)$$

Similarly, multiplying (18) by a test function ρ^\dagger and integrating over the domain leads to:

$$\forall \rho^\dagger, \quad \int_{\partial\hat{\Omega}} \rho^\dagger \left(\hat{\rho} \hat{\nabla} \hat{\varphi} + \frac{\hat{\nabla} \hat{\rho}}{Pe} \right) \cdot \mathbf{n} - \int_{\hat{\Omega}} \left(\hat{\rho} \hat{\nabla} \hat{\varphi} + \frac{\hat{\nabla} \hat{\rho}}{Pe} \right) \hat{\nabla} \rho^\dagger = 0 \quad (26)$$

Note that owing to the penalization method, the boundary condition (4) is only imposed in a weak way: Eq. (25) is actually equivalent to (17) with a modified

AED force & current

7

boundary condition $\hat{\varphi} + \varepsilon_p \mathbf{n} \cdot \hat{\nabla} \hat{\varphi} = 0$. We select $\varepsilon = 10^{-30}$ so that in practice the boundary condition is correctly verified. The same method cannot be used to enforce the boundary condition at the emitter as an integral over Γ is already present in (25). Inspired by [29] we introduce the Lagrangian multiplier

$$\lambda = \left(\hat{\rho} \hat{\nabla} \hat{\varphi} + \frac{1}{Pe} \hat{\nabla} \hat{\rho} \right) \cdot \mathbf{n} \quad \text{on } \Gamma \quad (27)$$

From the nul contribution of $\partial\Omega^E$ boundaries, using (27) in (26) leads to

$$\forall \rho^\dagger, \quad \int_{\hat{\Gamma}} \rho^\dagger \lambda + \int_{\partial\hat{\Omega}^c} \rho^\dagger \left(\hat{\rho} \hat{\nabla} \hat{\varphi} + \frac{\hat{\nabla} \hat{\rho}}{Pe} \right) \cdot \mathbf{n} - \int_{\hat{\Omega}} \hat{\nabla} \rho^\dagger \cdot \left(\hat{\rho} \hat{\nabla} \hat{\varphi} + \frac{\hat{\nabla} \hat{\rho}}{Pe} \right) = 0 \quad (28)$$

Boundary condition (19) is then enforced by introducing a test function λ^\dagger , leading to:

$$\forall \lambda^\dagger, \quad \int_{\hat{\Gamma}} \lambda^\dagger (\hat{\varphi} - 1) = 0 \quad (29)$$

2.4. Regularization

As in [21] we encountered difficulties for the Newton iterations to converge. We found convergence very sensitive to the mesh discretization and refinement at the emitter nearby Γ , as well as to the field discretization choice (as illustrated in next section). As identified by [21], the problem can be associated to the strongly hyperbolic nature of the problem. Our formulation already contains a diffusion term with small amplitude $1/Pe$ which makes the problem formally elliptic and therefore can be expected to act as a stabilization term, but this term does not seem sufficient to fully stabilize the formulation.

To overcome those difficulties we propose a new regularization method, which consists of replacing condition (19) over Γ by

$$\hat{\varphi}|_{\Gamma} = 1 + \varepsilon_\lambda \frac{\partial^2 \lambda}{\partial s^2} \quad (30)$$

where s stands for the curvilinear coordinate along Γ . Variational form of (30) then reads

$$\forall \lambda^\dagger, \quad \int_{\hat{\Gamma}} \lambda^\dagger (\hat{\varphi} - 1) + \varepsilon_\lambda \int_{\hat{\Gamma}} \frac{\partial \lambda}{\partial s} \cdot \frac{\partial \lambda^\dagger}{\partial s} = 0 \quad (31)$$

Equations (25), (28) and (31) are discretized using finite elements and the resulting non-linear problem is solved using a Newton method (detail are given in Appendix C). Mesh generation and adaptation, as well as resolution of the variational problems is performed using FreeFem++ version 4.5 [31]. Loops over parameters and generation of figures are done in the Matlab environment thanks to the drivers of the StabFem project [32].

3. Numerical validations

This section provide various validation tests. The sensitivity of the mesh refinement nearby the emitter, the advantages of using mesh refinement, the choice of finite-element polynomial base for each field, and the effect of regularization terms are analyzed.

3.1. Axi-symmetric test cases

We illustrate in Fig. 2 the interest of the regularization technique introduced above. Without regularization, the convergence is difficult to reach. If successful the resulting solution displays a very irregular ion density distribution characterized by radial "spikes" (Cf. Fig. 2a). The introduction of regularization completely suppresses this spurious numerical issue (Fig. 2b).

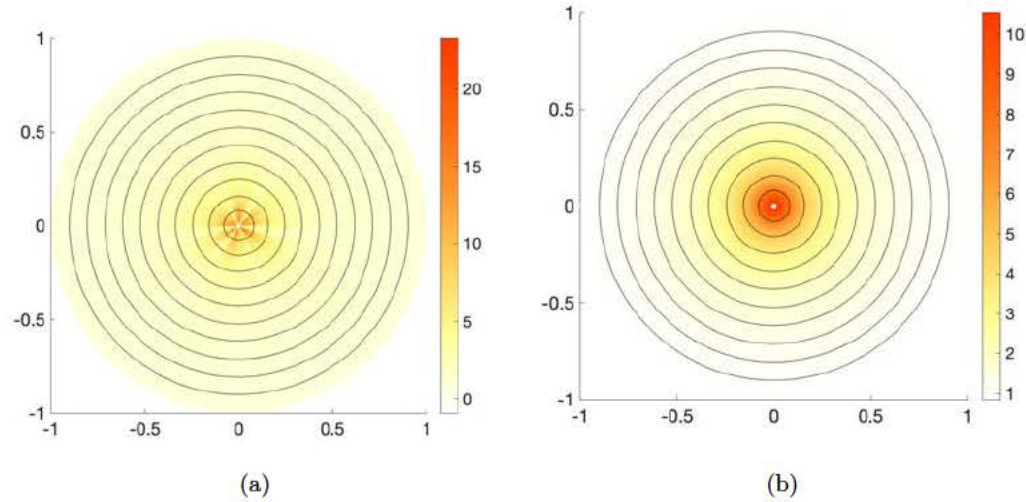


Figure 2: Ion density ρ (colors) and electric potential φ (iso-levels) computed (a) without regularization term ($Pe = 10^8; \varepsilon_\lambda = 0$) and (b) with regularization term ($Pe = 10^8; \varepsilon_\lambda = 10^{-8}$).

We also performed several tests in order to investigate which combination over finite element discretization P_k , $k = 1, 2, 3$, could provide the best precision, and finally reached the conclusion that (P_3, P_2, P_1) for (φ, ρ, λ) is the best choice, i.e the one chosen in Fig B1(Cf. Appendix B).

3.2. 1E/1C test case

This section illustrates the numerical predictions in a one emitter/one collector (1E/1C) configuration. We select the geometry with $r_e = 50\mu$, $R_{col} = 15mm$, $D = 30mm$, a configuration considered experimentally in [3]. As previously explained, lengths are non-dimensionalized so that the collector radius is unity. The domain full dimension $L \times L$ is chosen as being two-hundred times the collector one, i.e $L = 200$ in order to avoid finite size effects. We test many intermediate values for L whilst estimating quantities of interest (e.g current intensity, thrust etc.) and we found that for $L > 15D$, the finite domain effect was smaller than 0.5%. Figure 3 displays the structure of the solution (ion density, electric potential and electric field). Plot 3(a) is very close to the onset voltage leading to ionization, here $V = 6.47kV$ (or $\hat{E}_a = 38.5$, $\hat{\varphi}_a = 0.026$ in dimensionless variables). Up to this value, the ion density becomes non zero. Figure 3(b) is for $= 20kV$ ($\hat{E}_a = 12.45$, $\hat{\varphi}_a = 0.080$), for which the corona discharge is triggered, so that a flux of ions is expelled from the emitter down to the collector.

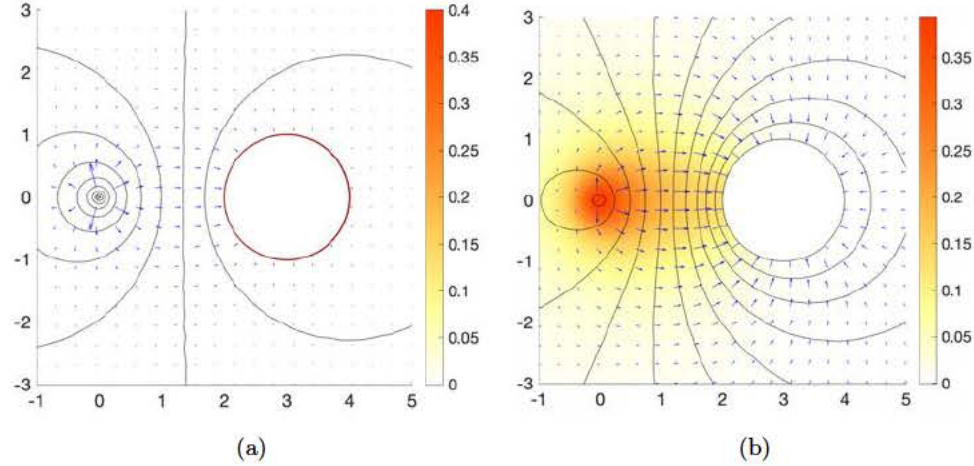


Figure 3: Ion density \hat{I} (color levels), electric potential $\hat{\phi}$ (isolines) and electric field \hat{E} (vectors) corresponding to 1E/1C case with $r_e = 50\mu m$, $R_{col} = 15mm$, $D = 30mm$, for (a) $V = \varphi_s = 6.47kV$ very close, and above the onset voltage (b) $V = 20kV$ where the corona discharge is triggered.

Figure 4(a) displays the computed dimensionless electric current \hat{I} versus the dimensionless voltage $\hat{\varphi}_a = V/(R_{col}E_a)$. As expected, the current is non-zero only above the threshold voltage. In fact, figure 4(a) depicts both the current emitted at emitter and the one collected at collector, but since they are very close (differing by less than 0.1%) the two curves can hardly be distinguished.

Figure 4(b) displays the Electro-AeroDynamic force T_{EAD} . As explained in sec. 2.1.3 it is possible to distinguish its respective contribution onto the emitter and the collector, using (13) both being displayed in Figure 4(b). Below the threshold, the two forces cancel resulting in a zero net force. In this range of operation, since there is no ion density, the electric charge on the emitter is exactly the opposite of the one at the collector. These mirror opposite charges exert onto each-other an opposite force, the sum of which being zero. On the other hand, above the threshold (FP- \hat{I} DF PLEASE GIVE VALUE HERE) [33], the figure indicates that the force exerted on the collector is enhanced whilst the one on the emitter is decreased, leading to a net force in the positive direction. In this range, the negative charge is still located uniquely by the collector, while the positive charge is located in parts on the emitter and in parts into the plasma. It is hence not surprising that the force exerted onto the emitter is reduced. Overall, the most dominant contribution of the propulsive force acts at the collector, as also found in [16].

3.3. Effect of regularization terms ε_λ and Pe

We now detail the effect of the regularization terms presented in our formulation, in order to select relevant values for the associated parameters.

Figure 5 displays the values obtained for the intensity and force when varying the parameter ε_λ . As can be seen two different regimes are obtained, with a transition in the range $\varepsilon_\lambda \approx 10^{-9}$. Moreover, for $\varepsilon_\lambda \leq 10^{-11}$, the computation does not converge

AED force & current

10

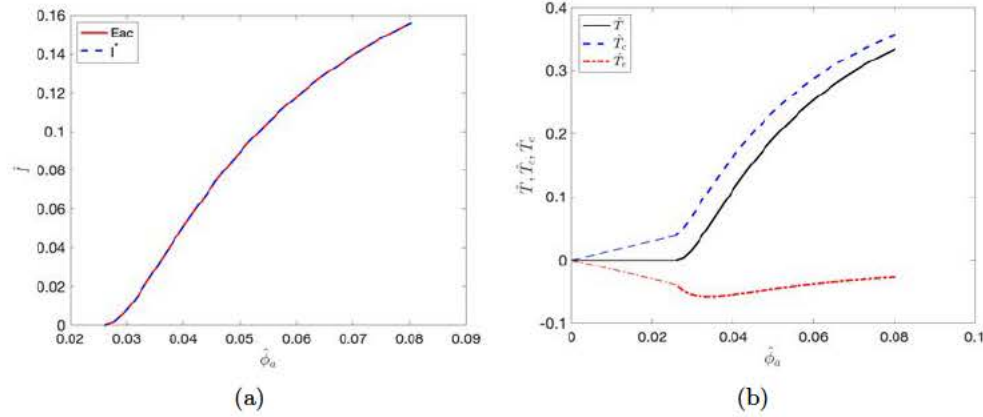


Figure 4: (a) Dimensionless intensity versus dimensionless applied voltage for 1E/1C case with $r_e = 50\mu m$, $R_{col} = 15mm$, $D = 30mm$. (b) Dimensionless electroAeroDynamic force versus applied voltage for the same configuration, and contributions of both electrodes.

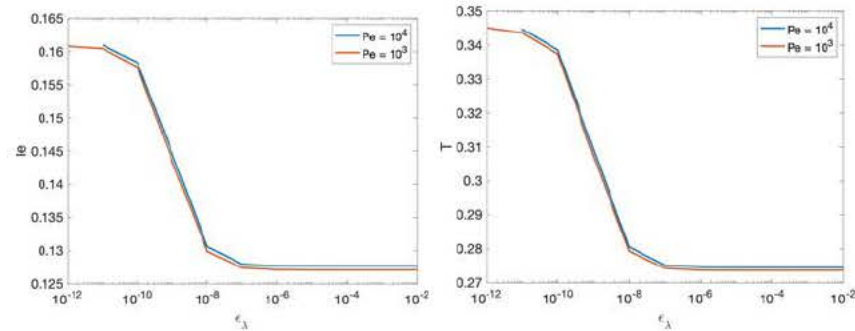


Figure 5: Effect of the regularization parameter ϵ_λ and Pe on the computed solutions. (a) Emitted Current (b) Complete Thrust.

any more, except if the Péclet number remains moderate. Since the values of force and intensity are notably different in both regimes, we analyse the structure of the ion density in the vicinity of the emitter in order to identify which ones corresponds is physically relevant. Figure 6 shows that with $\epsilon_\lambda = 10^{-8}$ the ion density remains isotropic in the vicinity of the emitter, while $\epsilon_\lambda = 10^{-12}$ this almost isotropic behaviour is broken leading to an almost dipolar ejection of charges. This second solution is non-physical regarding the known mono-polar character of the charge ejection nearby the emitter. To make sure to remain in a physical regime, we selected the value $\epsilon_\lambda = 10^{-4}$ for all our computations. Finally, figure 5 also illustrates the effect of the second regularization number Pe on the results. The results show that an asymptotic regime is obtained for $Pe \geq 10^4$. In the sequel we stick to the value $Pe = 10^4$ which warranties that this parameter has no effect on the results. Note that the value $Pe = 10^4$ is certainly much smaller than the physical value based on the ion diffusivity. However,

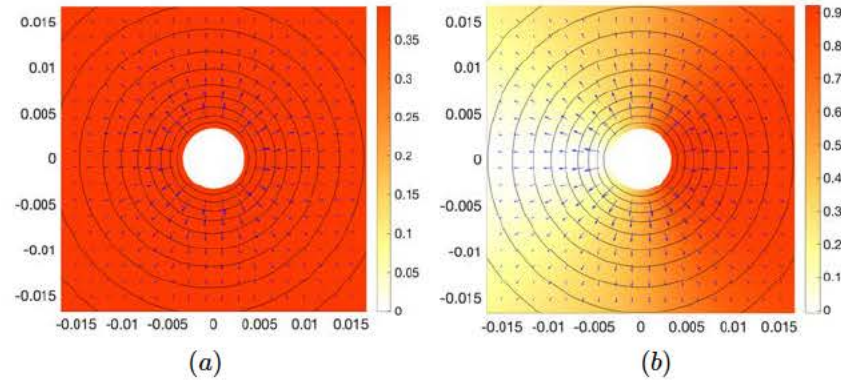


Figure 6: Effect of the regularization parameter ε_λ on the structure of the computed solutions nearby the emitter. Same conventions as Fig 3. (a) $\varepsilon_\lambda = 10^{-8}$ (b) $\varepsilon_\lambda = 10^{-12}$.

since in our code this parameters plays mostly the role of a stabilization term, there is no issue using a value closer to a real physical value.

4. Comparison with experiments

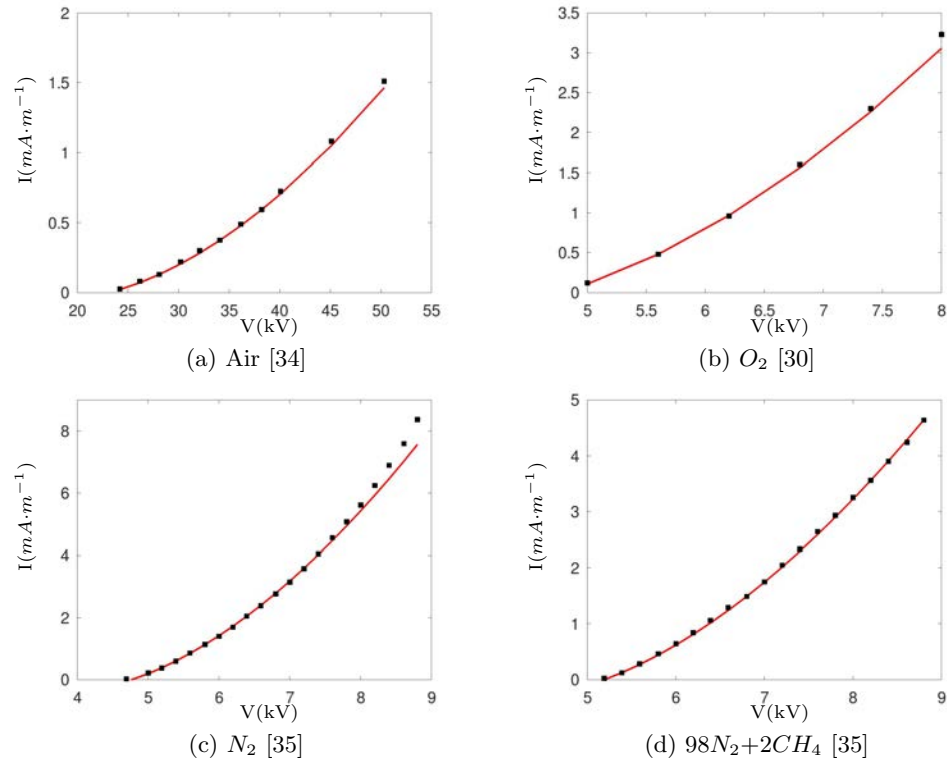
4.1. Axi-symmetric configurations

Experimental results are available in the literature considering axi-symmetric configurations [34, 30, 35]. A comparison of our computations with the available data is presented here. Of course, this geometry does not lead to any thrust force, so we only compare results for the current intensity.

As can be seen in Fig. 7, the numerical solution provides very accurate predictions to the experiments. This conclusion is similar to that of (8) who used the analytical solution of the problem recalled in appendix A. The various gas conditions and their respective parameters are provided in Table 1. In the table, we also provide the predictions of the discharge electric field predicted by Eqs. (7) (Peek's classical law) and (8) (asymptotic prediction from [23]). In air, the two expressions give comparable values up to 3%. In other gaz, Peek's prediction is not applicable, so the value is given as indicative in parentheses. The asymptotic prediction of [23] differs by up to 13% in N_2/CH_4 gaz mixture. In the sequel, we use formula (8).

Ref.	[34]	[30]	[35]	[35]
gaz	Air	O_2	N_2	$98N_2 + 2CH_4$
r_{col} [m]	$1.03 \cdot 10^{-1}$	$1.1 \cdot 10^{-2}$	$8e - 3$	$8 \cdot 10^{-3}$
r_e [m]	$7 \cdot 10^{-4}$	$6.25 \cdot 10^{-5}$	$6.25 \cdot 10^{-5}$	$6.25 \cdot 10^{-5}$
E_i [V/m]	$2.09 \cdot 10^7$	$1.99 \cdot 10^7$	$2.12 \cdot 10^7$	$2.16 \cdot 10^7$
β [m^{-1}]	$7.20 \cdot 10^5$	$1.15 \cdot 10^6$	$6.35 \cdot 10^5$	$7.26 \cdot 10^5$
γ	$2 \cdot 10^{-3}$	$1 \cdot 10^{-6}$	$5 \cdot 10^{-4}$	$4 \cdot 10^{-5}$
μ_p [$m^2 V^{-1} s^{-1}$]	$1.86 \cdot 10^{-4}$	$2.47 \cdot 10^{-4}$	$2.25 \cdot 10^{-4}$	$1.56 \cdot 10^{-4}$
E_{peek} [kV/mm]	6.71	(15.2)	(15.2)	(15.2)
E_a [kV/mm]	6.48	14.7	15.7	17.1

Table 1: Geometry and gas parameters for experimental references (axisymmetric configurations).

Figure 7: Comparison between prediction (continuous red line) and measurements (green dots) for current Intensity I versus applied voltage V (here $r_\Gamma = r_e$) for various gas composition.

4.2. 1E/1C configurations

We now present results of our numerical modeling for a number of 1E/1C (single emitter/single collector) for geometrical parameters corresponding with experimental databases from the literature [3, 4, 7]. As for the electric field at the emitter, we used either the Peek law (7) or the asymptotic formula (8) with values of E_{ief} , β_f and $K = \log(1 + \gamma^{-1})$ given by [36] which, according to [23], give very similar results in the range $r_e \in [10\mu\text{m}, 50\mu\text{m}]$. In all cases, we set the ion mobility to $\mu = 2 \cdot 10^{-4} \text{m}^2 \text{V}^{-1} \text{s}^{-1}$. In fact we found in the literature various value reported from $\mu = 1.554 \cdot 10^{-4} \text{m}^2 \text{V}^{-1} \text{s}^{-1}$ [5] to $\mu = 3 \cdot 10^{-4} \text{m}^2 \text{V}^{-1} \text{s}^{-1}$ [4]. This is because the ion mobility depends on the electric field [37]. In the considered range of electric field E (from 1.10^6 to 1.10^7V/m) it reduces from about $2 \cdot 10^{-4}$ down to $5 \cdot 10^{-5} \text{m}^2 \text{V}^{-1} \text{s}^{-1}$. In the present contribution we have kept a constant mobility as a first approximation, as done in many other contributions [14, 15, 16, 17, 18, 19, 9]. Rather than trying to adjust this parameter to fit each experimental dataset, we prefer to adopt an intermediate value for all cases.

Figures 8a, 9a, 10a and 11a display the computed Intensity-Voltage (I-V) curves and compares with experiments. The comparison shows that the I-V curve prediction matches remarkably well with the experimental measurements. More generally, and, and least for low voltage, the prediction for I-V curves of Figures 9a, 10a and 11a are very good. More precisely, concerning the set $D = 30\text{mm}$, $R_c = 15$, $r_0 = 50\mu\text{m}$, of Figure 9a, in a subsequent publication [33] indicate a critical voltage for the onset of corona discharge $V_c = 5.86 \text{kV}$. Our computations, performed into a domain size $L = 15D$ with Neumann boundary conditions indicate a threshold 6.51kV , about 10% larger. Diminishing the domain size to $L = 4D$ and using Dirichlet lateral boundary conditions as in [33] leads to 2% difference, a very satisfactory agreement. Since no fitting parameter are used to obtain these results for which the exact experimental geometrical parameters are used, it is thus interesting to observe that numerical predictions very significantly permit to capture the electrical response of corona discharge from drift-region modeling only, using Kaptzov approximation. More precisely, the maximum observed discrepancy is found for the dataset where $R_{col} = 5\text{mm}$, $D = 30 \text{mm}$ of Figure 9a where it reaches 25%.

Two arguments may be raised to explain the observed discrepancy. A first explanation is the possible existence of leak currents. Such leak currents are unavoidable in experiments, but they are not present in our simulations considering our choice of boundary conditions. This explanation is consistent with the fact that in most cases the numerical predictions underestimates the experimentally measured currents. A second possibility is the effect of the ion mobility. As explained above, we adopted a value $\mu = 2 \cdot 10^{-4} \text{m}^2 \text{V}^{-1} \text{s}^{-1}$ in all cases. According to (22), the intensity is directly proportional to μ , so a larger effective ion mobility may also explain the underestimation of intensity by our simulations.

Let us now compare the predictions and experimental measurement for the thrust force. Figures 8b, 9b, 10b and 11b display the thrust T per unit length in the span-wise direction versus of either the voltage V or the intensity, depending upon which of these representations is favoured in the experimental references. Although our numerical computations correctly predict the trends in a qualitative way, they over-predict, in every case, the observed thrust. The observed discrepancy remains however moderate and of comparable magnitude in all cases, i.e in between 20 to 30%. In the worst case, for the case $D = 20\text{mm}$ considered by [3], over-prediction reaches 50% (Figure 8b).

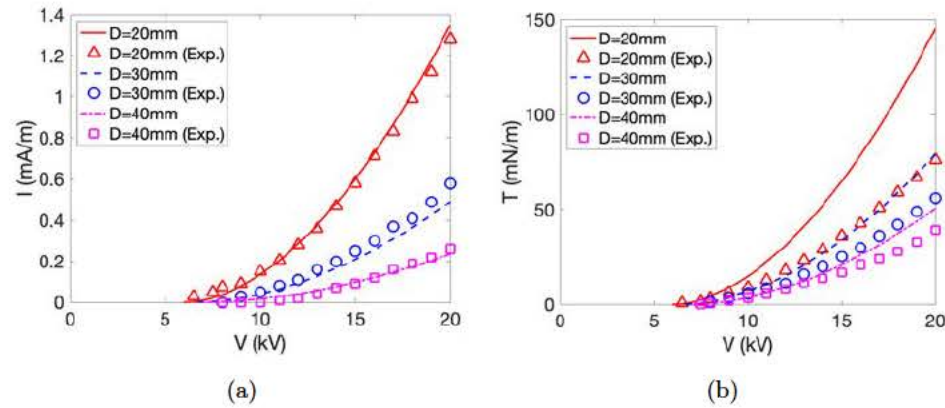


Figure 8: (a) Intensity and (b) Thrust force versus the applied voltage for $R_{col} = 15\text{mm}$, $r_0 = 50\mu\text{m}$ and several values of gap D . Comparison with experimental data by Kiouisis et al. [3]

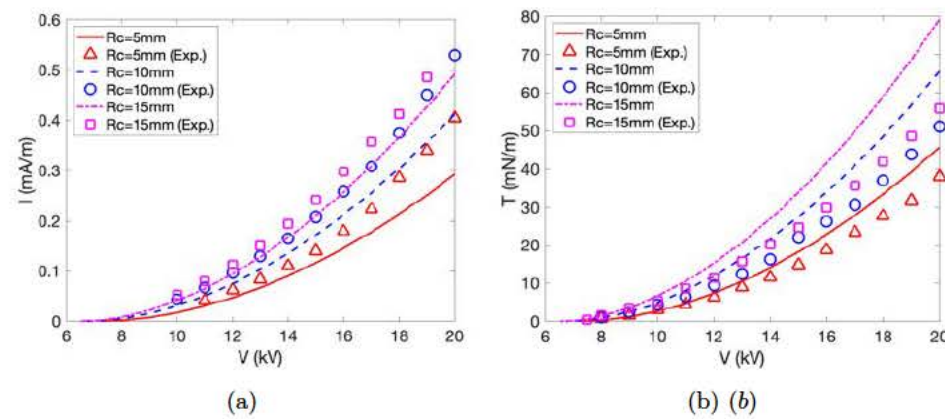


Figure 9: Results for 1E1C configuration. (a) Intensity and (b) Thrust force versus the applied voltage for $D = 30\text{mm}$, $r_0 = 50\mu\text{m}$ and several values of collector radius R_{col} . Comparison with experimental data by Kiouisis et al. [3]

This systematic discrepancy may be attributed to the fact that in experiments, the measured net thrust force T is not solely the ElectroAeroDynamics thrust T_{EAD} but also contains an aerodynamic force D_{aero} corresponding to the drag exerted onto the collector by the ionic wind generated by the electrodynamic force. These forces act in opposite directions ($T = T_{EAD} - D_{aero}$) hence it is normal that the total force measured in experiments is smaller than the computed T_{EAD} . Considering that the I-V response prediction is a good indicator of the modeling hypothesis for the electric phenomena, and since the electro-propulsive prediction is a by-product of this electrical modeling, it is very tempting to attribute the observed systematic over-estimation of the propulsive deviation to the aerodynamic drag contribution. However, it is already interesting to observe that keeping with electric computation only, one is able to

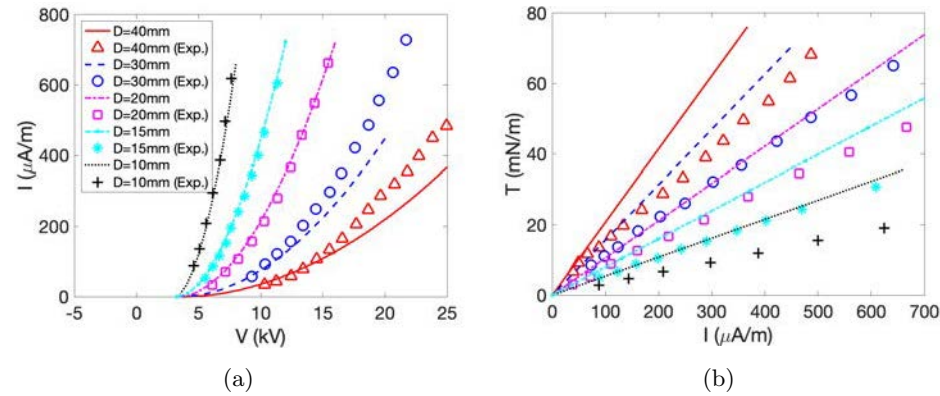


Figure 10: Results for 1E1C configuration. (a) Intensity and (b) Thrust force (same legend as (a), hence not duplicated) versus the applied voltage for $r_c = 6\text{mm}$, $r_0 = 12.5\mu\text{m}$ and several values of gap D . Comparison with experimental data by Moreau et al.

provide a relevant estimate of the propulsive thrust.

Predicting the drag D_{aero} would require resolution of the Navier-Stokes equations with a volumic forcing term corresponding to the Coulomb force. This point falls outside of the scope of the present paper, which focusses only on the electrostatic problem. We can, however, estimate the order of magnitude of this drag using dimensional analysis. Noting U the order of magnitude of the drift velocity, the order of magnitude of the acceleration term in the Navier-Stokes equations is U^2/D . Equating this order of magnitude with that of the Coulomb force ρ^*V/D (ρ^* being the order of magnitude of the ion density estimated here as $\rho^* \approx \varepsilon_0(V - V_c)/D^2$) leads to the estimation $U \approx \sqrt{\varepsilon_0 V(V - V_c)}/D$. Assuming an aerodynamic drag scaling as $D_{aero} = \rho R_{col} U^2 C_d$ where C_d is a drag coefficient of order one leads to:

$$D_{aero} \approx \frac{\rho R_{col} \varepsilon_0 V(V - V_c)}{D^2}. \quad (32)$$

Considering the present configurations with $R_{col} \approx 10\text{mm}$, $V \approx 20\text{kV}$, $V_c \approx 10\text{kV}$, $D \approx 30\text{mm}$, these order-of-magnitude estimations lead to $U \approx 1.4\text{m/s}$ and $D_{aero} \approx 25\text{mN}$, which is effectively comparable with the order of magnitude of the observed force. To complete the discussion on 1E/1C configurations, Figures 11(c - d) display the intensity I and the surfacic thrust T/D versus of the equivalent electric field V/D . For both quantities, the collapse of data along a single curve is confirmed as observed in [7]. Here again, apart from a moderate shift in thrust for $V/D > 6\text{kV/cm}$, the scaling and behaviour of the predicted thrust is both physically sound and a fair prediction.

4.3. 1E2C configurations

Here we consider a one emitter//two collectors (1E/2C) configuration (Cf Fig 1b) studied in [7] where the spacing s between the collectors is a new geometrical parameter. A motivation of this configuration in [7] was to confirm the existence of an

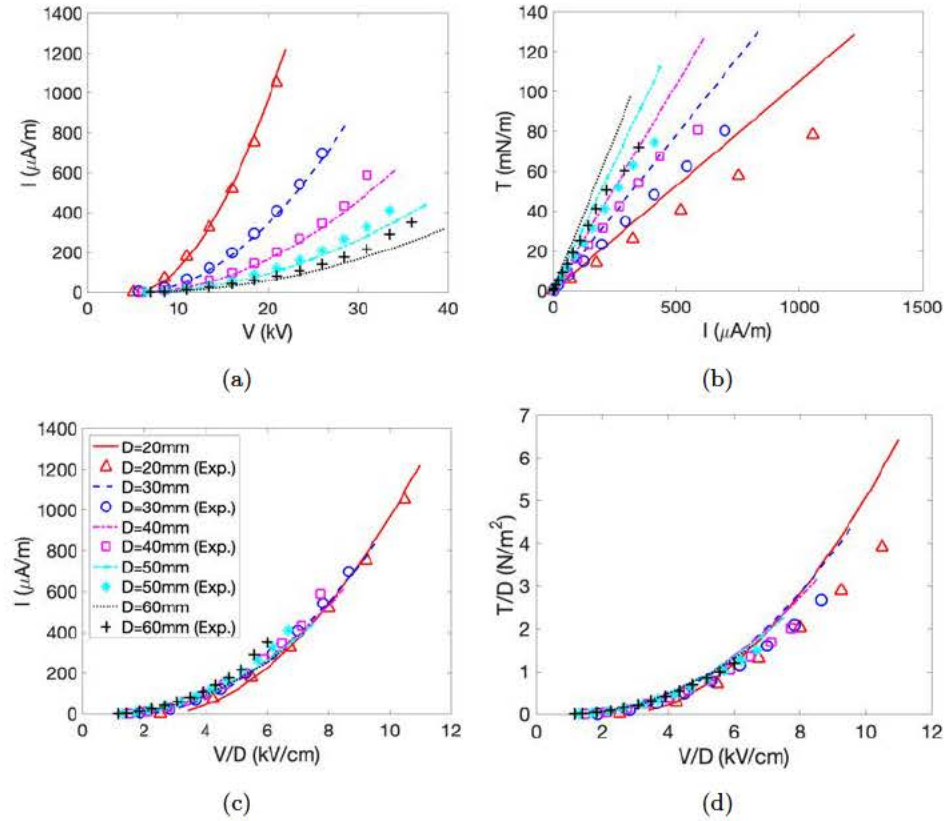


Figure 11: Results for 1E1C configurations with $r_c = 5\text{mm}$, $r_0 = 25\mu\text{m}$ and several values of gap D . Comparison with experimental data by Monrolin et al. All panels a,b,c,d share the same legend as (c), hence, not duplicated.

optimal spacing leading to a maximal thrust, and to provide the corresponding gain in performance. Here we compare the predictions for various emitter/collector distances $D = 2, 5, 9\text{mm}$ and one spacing between collectors $s = 8\text{mm}$, the I-V curve, the thrust and the Thrust-to-power ratio with experimental measurements in Figures 12a,b,c,d. Concerning the $I - V$ curve of figure 12a, the comparison between the measurements and the prediction is very good for the shortest distance ($D = 2\text{mm}$), with a slight degradation (25%) for the largest distance at highest potential. Concerning the thrust prediction depicted in figure 12b, a maximum of 10% difference between the numerical predictions and the measurements is observed. This distinct improvement for matching thrust experiments with numerical prediction in this 1E/2C configuration compared to 1E/1C (discussed in the previous section), might again be understood as resulting from a distinct aerodynamic drag. As a matter of fact, it is known from [28] that, since the ionic wind velocity transverse profile downstream from the emitter but upstream from collectors are peaked near the centre, i.e along the horizontal line passing through the emitter, the main momentum transfer to the flow by the charge flux passed in-between the collectors, resulting in a lower drag than in the 1E/1C case. This result in a better prediction when omitting the drag.

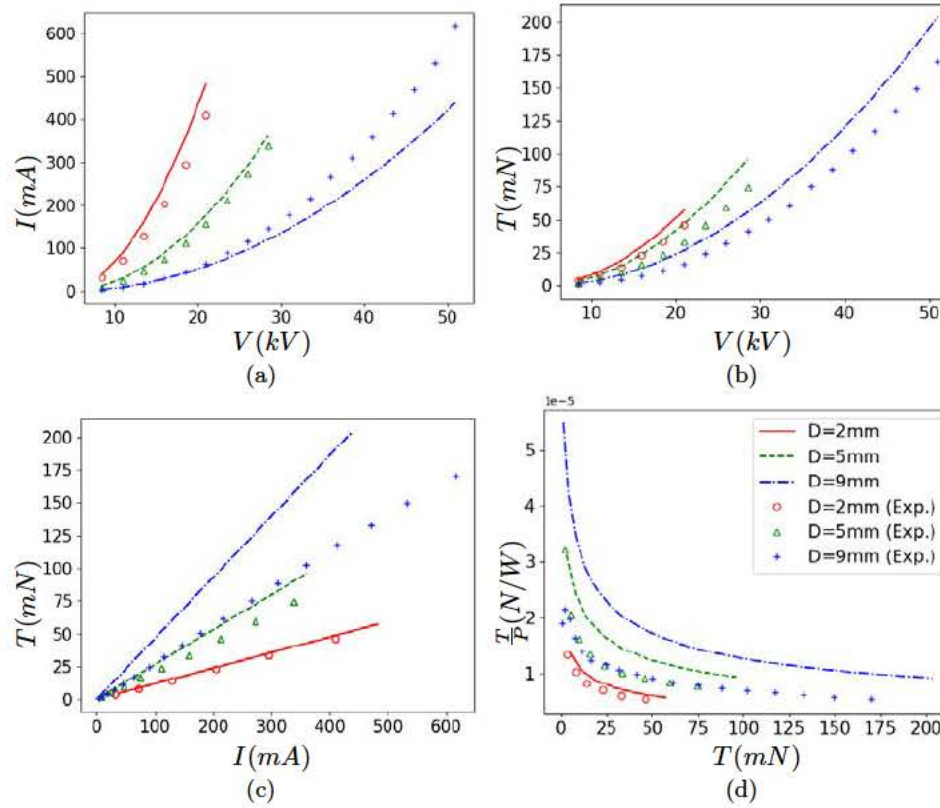


Figure 12: Results for 1E2C configurations with $r_c = 5mm$, $r_0 = 25\mu m$, vertical spacing $s = 8mm$ and several values of gap D . Comparison with experimental data by Monrolin et al. [7]. All panels a,b,c,d share the same legend as (d), hence, not duplicated.

4.4. 2E2C configurations

We now examine a 2E2C configurations studied in [5] (Cf Figure 1c) in Figures 13 and 14.

Figures 13a,b compare the I-V curve and the thrust with various applied potential and various transverse distances Δ between the emitter and the collectors. Again, in this case, the matching between predictions and experiments is remarkably good with less than 10% differences for the predicted current as well as the predicted thrust. One can notice in Figure 13b that, for small current, the expected linear scaling $T \sim I$ is found in the numerical simulations, but not in the experiments. It is indeed expected that experimental difficulties arise when trying to evaluate very low currents. + In figure 14, we plot the computed intensity I and Thrust T versus the electrode spacing Δ for three separation values. Except in plot 14d, the computations are done considering a constant electric field $V/D = 4.5V/cm$, in order to obtain intensities and thrusts in a similar range. For large Δ/D ratio, one expects a 'decoupled 1E/1C limit' to arise for which the system behaves as a collection of independent emitter/collector

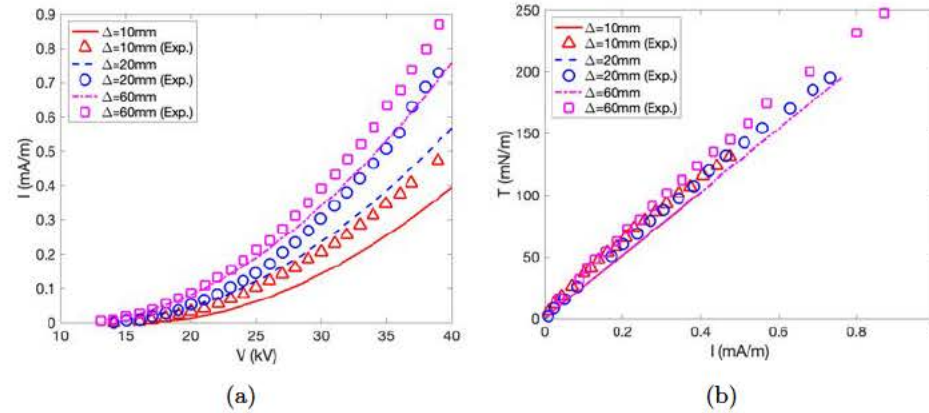


Figure 13: (a) Intensity versus applied Voltage and (b) Thrust Force versus Intensity for 2E2C configurations, with $r_c = 3.175\text{mm}$, $r_0 = 110\mu\text{m}$, $L = 50\text{mm}$ and several values of vertical gap H . Comparison with experimental data by Gilmore & Barrett [5].

pairs. This is indeed what is observed in Figure 14a,b where a plateau is reached at large D values. In the subsequent figure 14c T_{EAD} is rescaled by its value T_{1E1C} in the corresponding 1E/1C configuration, so that one can observe a collapse of the various curves to reach the same plateau value of 2 in the limit $\Delta/D \gg 1$, as expected from the addition of two decoupled 1E/1C configurations. Interestingly, all curves display an overshoot, so that for $\Delta/D \approx [1 - 2]$ the intensity and thrusts of the configuration are larger than those corresponding to two independent pairs. This rescaling of figures 14c also permits to more precisely observe the performance degradation in the opposite limit $\Delta/D \ll 1$, which was initially a motivation of [5] for performing these measurements.

Figure 14(d) presents another rescaling by the thrust for $\Delta/D = 1$, as done by [5]. To fit with this reference, we considered in this case a single tension $V = 38\text{kV}$ rather than a constant electric field. Gilmore & Barrett [5] obtained a least-square fit of their experimental data with the following law (Eq. 4.1 of their paper): $T/T_{\Delta/D \approx 1} \approx 1.02(1 - e^{-4\Delta/D})$. As shown in figure 14(d), this law also provides a consistent fit to our numerical simulations but for the small overshoot underlined above. Note that in Fig. 5 of [5] overshoots with respect to the main curve can also be noticed for several data sets.

Finally, plots 14(e-f) display the thrust-to-power ratio T_{EAD}/P and the thrust density $T/(\Delta D)$ versus Δ (again for constant $V/D = 4.5\text{kV/cm}$). On the one hand, the Thrust-to-power ratio is found very poorly sensitive to parameters D and Δ , being in the range $[11.25 - 11.55]\text{mN/W}$ whilst they both vary by a large amount. On the other hand, we found that the thrust density is a decreasing function of Δ . This result differs from the conclusions of [5] who, thanks to a correlation of their data, reached the conclusion that the thrust density is maximized for $\Delta/D \approx 0.41$. This could be due to the fact that we did not include the drag contribution which might degrade the thrust for small spacing. Overall, for 2E/2C configurations, our predictions also permits to recover a very close comparison with experimental measurements. We thus

This is the author's peer reviewed, accepted manuscript. However, the online version of record will be different from this version once it has been copyedited and typeset.
PLEASE CITE THIS ARTICLE AS DOI: 10.1063/5.0041061

AED force & current

19

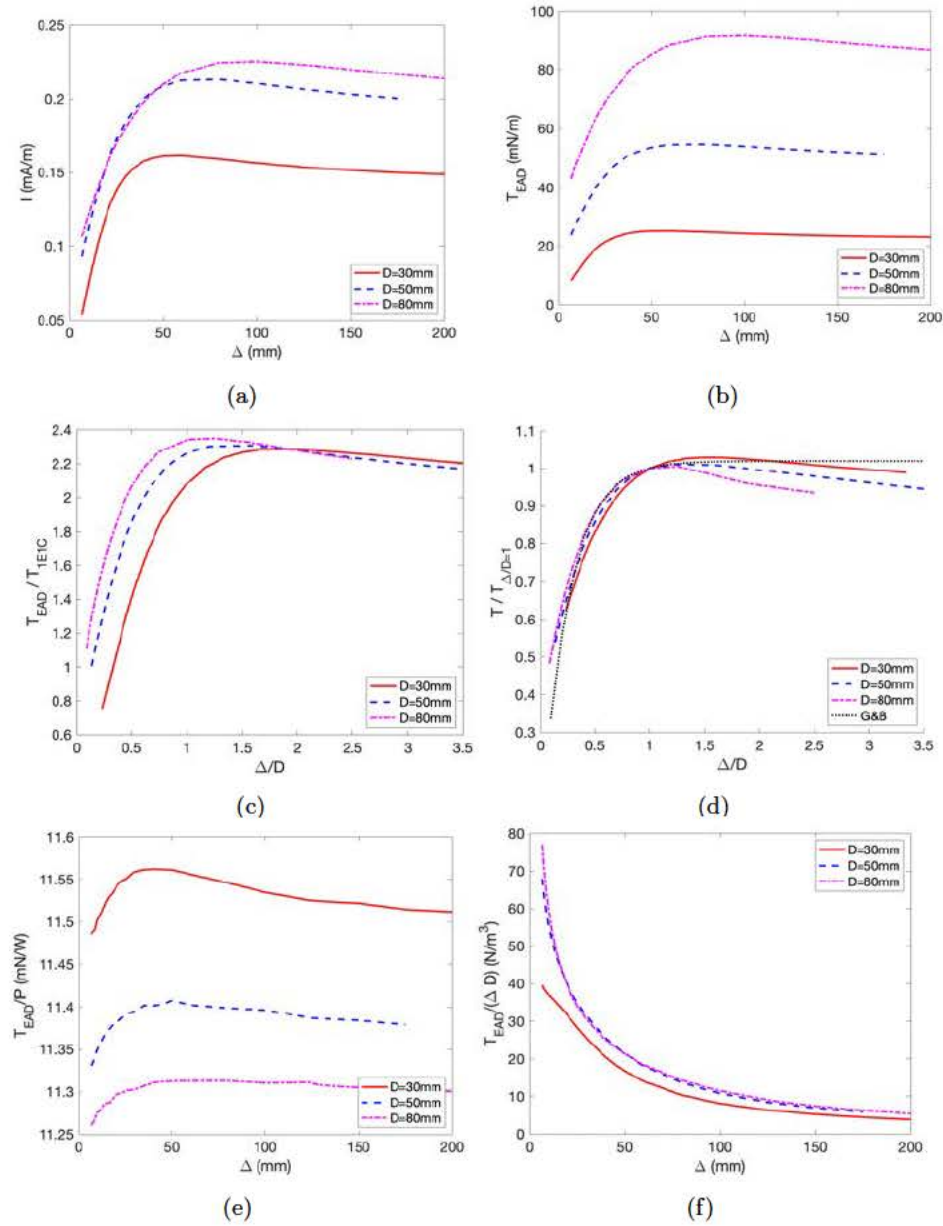


Figure 14: Results for 2E2C configurations when varying gap D and vertical spacing Δ . Electrode dimensions are $R_{col} = 3.175\text{mm}$, $r_0 = 39.95\mu\text{m}$. In (a – b – c – e – f) the applied potential is $V = 38\text{kV}$ for $D = 80\text{mm}$, $V = 22.5\text{kV}$ for $D = 50\text{mm}$ and $V = 13.5\text{kV}$ for $D = 30\text{mm}$ in order to maintain constant electric field V/D ; in (d) all configurations have $V = 38\text{kV}$.

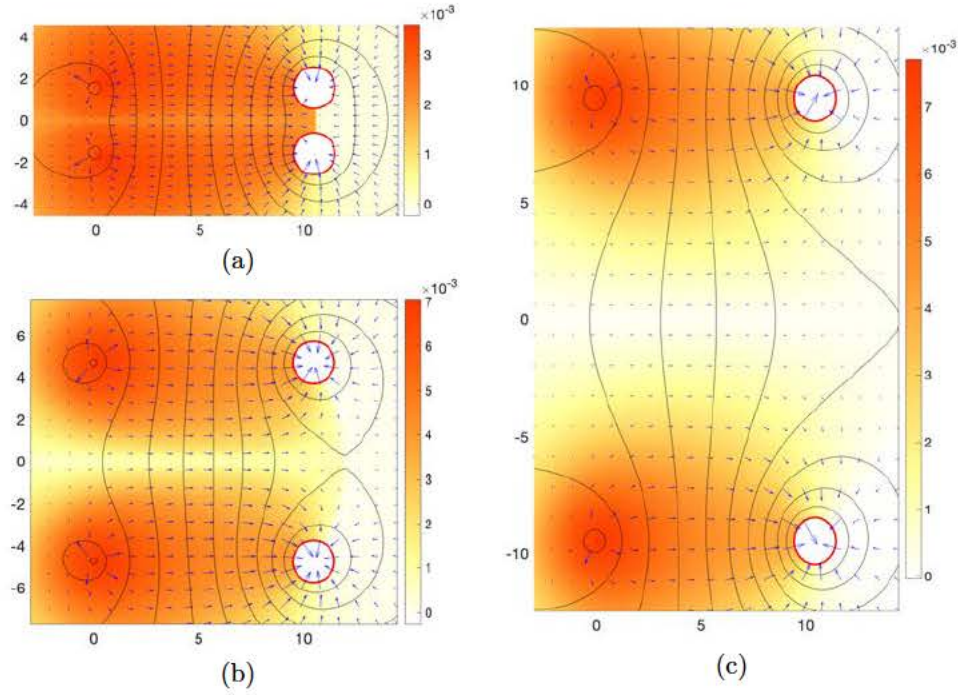


Figure 15: Nondimensional ion density $\hat{\rho}$, isopotential lines and electric field for 2E/2C configuration with $D = 30\text{mm}$, $V/D = 12\text{kV/cm}$, for (a) $\Delta = 10\text{mm}$, (b) $\Delta = 30\text{mm}$, (c) $\Delta = 60\text{mm}$.

reach the same conclusion as [1, 5] that the thrust density can hardly be increased by increasing the density of emitters.

Figure 15 displays the ion density, iso-potentials, and electric field for $D = 30\text{mm}$ and three values of Δ . For small Δ , a salient feature is the existence of a sharp front between the two collectors, where the ion density is almost discontinuous. This is not surprising since the ion density is governed by a strongly hyperbolic equation which allows such discontinuities. The front is located at the boundary between the front region where electric field lines carry charges from the emitter, and the back region where ions are absent. This sharp front is especially visible for small gap values for $\Delta = 10\text{mm}$ (plot 15(a)). For $\Delta = 60\text{mm}$ (plot 15(c), which corresponds approximately to the maximum thrust in figure 14(c), the sharp front is no longer visible and the structure is very similar to that of two decoupled electrode wires.

This is the author's peer reviewed, accepted manuscript. However, the online version of record will be different from this version once it has been copyedited and typeset.
PLEASE CITE THIS ARTICLE AS DOI: 10.1063/5.0041061

AED force & current

21

4.5. Periodic nE/nC configurations

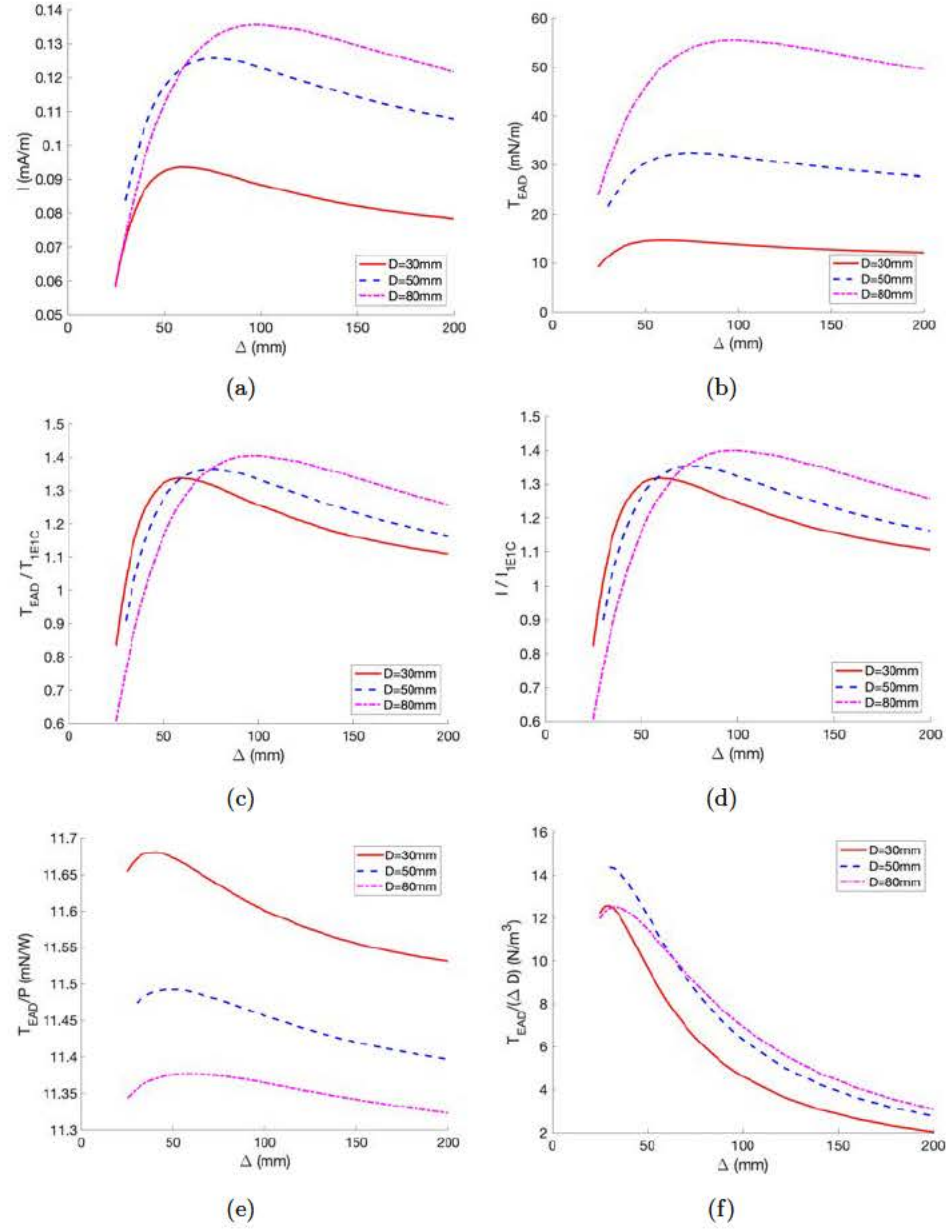


Figure 16: (a) Intensity and (b) Thrust force versus Δ/D in transversely periodic configurations, for periodic configurations, with $r_c = 3.175\text{mm}$, $r_0 = 39.95\mu\text{m}$, $V/D = 4.5\text{kV/cm}$.

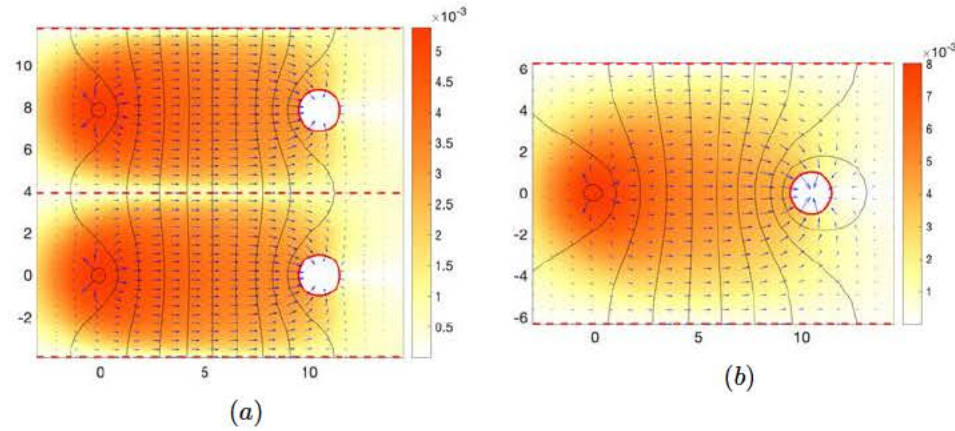


Figure 17: Nondimensional ion density $\hat{\rho}$, iso-potential lines and electric field for periodic configurations with $D = 30mm$, $V/D = 4.5kV/cm$. (a): $\Delta = 25mm$ (two elementary cells of the periodic pattern are shown); (b): $\Delta = 40mm$ (one elementary cell is shown).

To further investigate the issue of interaction between multiple electrode pairs, we now switch to fully periodic (nE/nC) configurations, in a transversely periodic domain (Cf Figure 1d). Figure 16 displays the thrust and intensity (for one elementary cell of the periodic pattern) along with a number of related quantities, as function of Δ for three values of D . As in the previous paragraph, the configurations are chosen with constant electric field V/D to obtain intensities and thrusts of comparable magnitudes. The overall behaviour for the intensity and the thrust versus Δ is similar with that observed in the previous paragraph for $2E/2C$ configurations, with the existence of an overshoot for intermediate values of Δ . However, this overshoot is much more pronounced than for $2E/2C$, as thrust and intensity of a periodic arrays can be 40% larger than an equivalent number of independent electrode pairs (see fig. 16c – d).

Considering thrust-to-power versus Δ (fig. 16e) leads to the same conclusions as for $2E/EC$ configurations. The obtained value is also weakly dependent upon D and Δ . For all cases a maximum can be detected in the range $\Delta \approx 45 - 60mm$, but the values in the explored range only vary within a few percents and remain close to those obtained for $2E/EC$ configurations, namely $T/P \approx 11mN/W$. On the other hand, regarding thrust density (Fig. 16f), an optimal value of Δ can now be detected. This optimal value is about $\Delta \approx 40mm$ for all values of D considered.

Finally, we note that for fully periodic configurations, the critical voltage leading to corona discharge is notably larger than for $1E/1C$ and $2E/2C$ configurations. Indeed, in the figure, the threshold is only reached above $\Delta \gtrsim 25mm$, while for $2E/2C$ discharge was already observed for $\Delta \approx 10mm$.

Figure 17 shows the structure of the solution for periodic configurations with $D = 30mm$ and $\Delta = 25mm$ (Cf Figure 17(a)) and $\Delta = 60mm$ (Cf Figure 17(b)). Note that the sharp front observed for $2E/2C$ in the ion distribution is no longer present. This is not surprising because electric lines are now symmetric and carry ions on both sides of the collectors. Hence the region with depleted ion density behind the collectors is no longer present.

5. Conclusion

In this work, we have described a numerical approach to compute the coupled electric field/ion distribution in various configurations of electrodes using a drift region modeling of corona discharge as in [20, 21, 18, 9]. We used a finite-element discretization using dynamically adapted meshes, and solve the non-linear equations with Newton iterations, a numerical strategy that we did not find previously used for this class of problems. A new stabilization term to enforce a uniform charge distribution around the emitters is introduced. The problem is solved in terms of nondimensional variables, which allows to express the problem in terms of a unique dimensionless parameter $\hat{\varphi}_a = V/(E_a R_{col})$. The method is efficient and robust, and easily applicable to various geometrical configurations.

After some validations for axi-symmetric configurations where an analytical solution is available, the method is used to predict the intensity I and thrust T for various configurations including $1E/2C$, $2E/2C$ and periodic nE/nC configurations. Systematic comparisons with results from several experimental databases [4, 3, 7, 5] have been performed curbing the possible influence of finite-size effects by using domain sizes fifteen time larger than emitter/collector distance D . The modeling is shown to correctly predict the experimentally observed trends. The method was generally found to under-predict the intensity current by about 10 – 20% and to over-predict the thrust by a similar amount. The results allow to quantify the efficiency of these configurations in terms of thrust-to-power ratio and thrust density, whereby our numerical predictions confirmed the trends observed in experiments.

In our analysis, we voluntarily stick to a resolution of the physical problem without adjustable parameters. We set the ion mobility μ to a widely used value in air, as well as used the admitted Peek's law for the electric field at emitters.

In this restrictive framework of uniform mobility, drift region approximation and without computing the ionic wind contribution to the drag force, we found a surprisingly close agreement (from 10% in the most favourable case to 40% in the worst one) between numerical predictions and various experimental configurations. We confirm the presence of some optimal configuration for thrust in emitters/collectors arrays being D apart, with an optimal separation distance Δ ranging from $\Delta = 1.1D$ to $\Delta = 1.3D$. The obtained results for the thrust is very convergent with previous experimental measurements [5] and data-fit but for the presence of a small overshoot at large distances. We also found a different optimal separation distance Δ for thrust density being poorly sensible to D and close to $\Delta \approx 40mm$, a conclusion partly shared from experiments [5] for which density is also maximum for smaller value of Δ , but linearly scaling with D as $\Delta \approx 0.41D$ [5]. Albeit the qualitative conclusions between finite size configurations and infinite periodic ones are very similar, some specific differences have been found and discussed.

Several parametric adjustments could certainly improve the matching with experiments, from adapting the mobility, taking into account its dependence with the electric field or adding some current leakage. This could easily improve the matching in terms of intensity, but will not influence the thrust prediction.

As for the thrust, the main source of discrepancy comes from the fact that our approach predicts the electro-aerodynamic thrust T_{EAD} while in experiments a total force is measured, containing both the EAD thrust and the aerodynamic drag of the electrodes due to ionic wind. A dimensional analysis argument confirms that the order-of-magnitude of drag force is indeed comparable to the difference between

our computed EAD thrust and the measured total thrust. This hypothesis could be confirmed by additional CFD computations, which should also consider various connected issues such as modeling and capturing the effect of flow non-stationarities on the drag (due to the wake), possibly modeling the effect, that we did not wish to consider in this study.

Acknowledgments

This work has been supported by the ANR-Astrid Grant 'PROPULSION' number ANR-20-ASTC-0029-02.

The data that support the findings of this study are available from the corresponding author upon reasonable request.

Appendix A. Analytical solution for axis-symmetrical case

In this appendix we reproduce the analytical solution for the axisymmetric configuration, as given in [30]. The collector is considered as a cylindrical shell of radius R_{col} surrounding the emitter wire with radius r_0 . We note $\hat{r}_\Gamma = r_0/R_{col}$.

Using our nondimensional formulation of the equations (and neglecting diffusion in (2), the electric potential $\hat{\varphi}(\hat{r})$ and charge density $\hat{n}(\hat{r})$ satisfy

$$\hat{\nabla}(\hat{n}\hat{\nabla}\hat{\varphi}) = 0, \quad (\text{A.1})$$

expressed in cylindrical coordinates,

$$\partial_r(\hat{r}\partial_r\hat{\varphi}) = 0, \quad (\text{A.2})$$

can be integrated introducing a constant J

$$\hat{\rho} = \frac{J}{\hat{r}\partial_r\hat{\varphi}}. \quad (\text{A.3})$$

Replacing this solution in (17) leads to

$$\frac{1}{\hat{r}}\partial_r(\hat{r}\partial_r\hat{\varphi}) = -\hat{\rho}. \quad (\text{A.4})$$

so that

$$\partial_r(\hat{r}\partial_r\hat{\varphi})^2 = -2\hat{r}J. \quad (\text{A.5})$$

So that finally introducing constant K

$$-\partial_r\hat{\varphi} = \frac{\sqrt{-J\hat{r}^2 + K}}{r} \quad (\text{A.6})$$

Integrating upon boundary condition $\hat{\varphi}(1) = 0$

$$\hat{\varphi}(\hat{r}) = \sqrt{J + K} - \sqrt{J\hat{r}^2 + K} + \sqrt{K} \log \left(\frac{\sqrt{J\hat{r}^2 + K} + \sqrt{K}}{\hat{r}(\sqrt{J + K} + \sqrt{K})} \right).$$

The charge density is then given by

$$\hat{\rho}(\hat{r}) = \frac{J}{\sqrt{J\hat{r}^2 + K}} \quad (\text{A.7})$$

AED force & current

25

Applying boundary conditions then leads to a couple of transcendental equations for J and K which have to be solved numerically to get the final solution :

$$(\hat{\varphi}_a)^{-1} = \frac{\sqrt{-J\hat{r}_\Gamma^2 + K}}{\hat{r}_\Gamma} \quad (\text{A.8})$$

$$1 = \sqrt{J + K} - \sqrt{J\hat{r}_\Gamma^2 + K} + \sqrt{K} \log \left(\frac{\sqrt{J\hat{r}_\Gamma^2 + K} + \sqrt{K}}{\hat{r}_\Gamma(\sqrt{J + K} + \sqrt{K})} \right) \quad (\text{A.9})$$

One can notice that $J = 0$ leads to zero charge density everywhere, a trivial solution for a purely conductive current. An solution exemple is presented in Fig. A1 together with the result of the numerical computation.

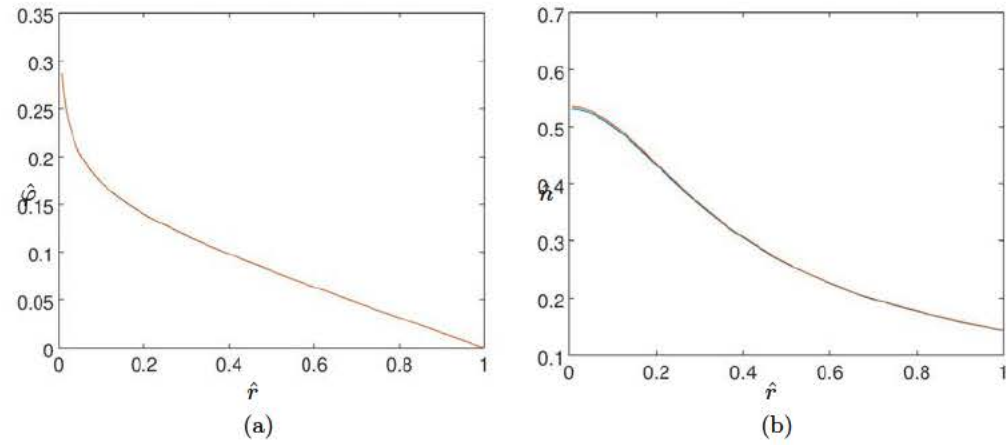


Figure A1: Comparison between the analytical solution in cylindrical configurations. (a) Electric potential $\hat{\varphi}(\hat{r})$ and (b) charge density $\hat{\rho}(\hat{r})$ for an axisymmetric configuration with $r_e/R_{col} = 0.001$ and $\hat{\varphi}_a = 0.28$. Analytical solutions (A.7) are superposed onto numerical solution using finite elements. The curves overlap very precisely so that they can hardly be distinguished.

Appendix B. Numerical convergence study and mesh refinement

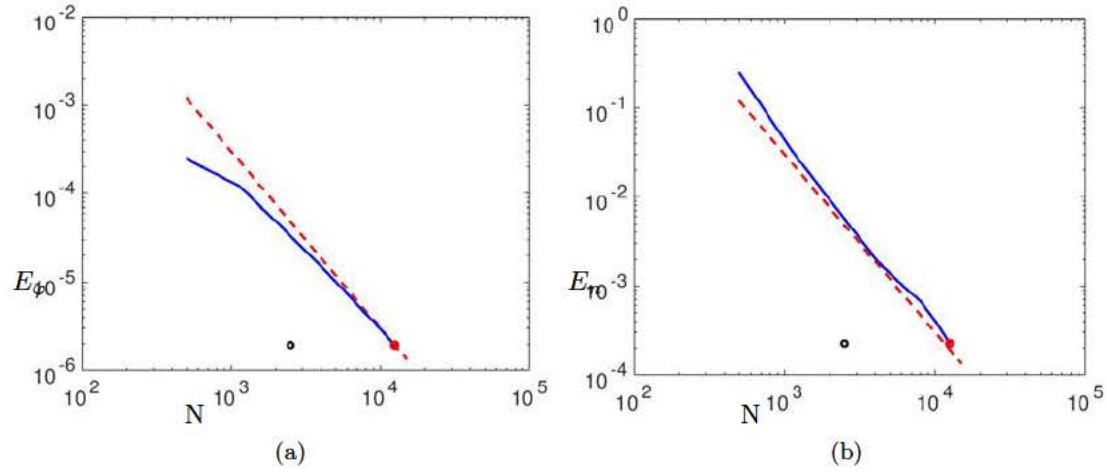


Figure B1: (a) \mathcal{L}_2 error on the potential, i.e. $E_\varphi \equiv \|\varphi_{th} - \varphi_N\|_{\mathcal{L}_2}$. (b) \mathcal{L}_2 error on the charge density, i.e. $E_n \equiv \|n_{th} - n_N\|_{\mathcal{L}_2}$. In both case a (P_3, P_2, P_1) finite element discretization is chosen for (φ, n, λ) . The red curve indicates a $1/N^2$ convergence behaviour. The black dot represents the result obtained with a mesh refinement technique (whose mesh is illustrated in Fig. B2a,b) providing a similar precision as the red dot.

We hereby discuss and illustrate the mesh convergence issues considering an axisymmetric test case (see Appendix A). Physically, this configuration correspond to a case where the collector is a cylindrical shell surrounding the emitter rather than a wire. Figure B1 plots the maximum error with respect to the analytical solution versus the number of mesh nodes N , considering first a collection of meshes generated by Delaunay triangularization, resulting in uniform mesh density. The figure indicates a numerical convergence with spatial order two. Rather than using a mesh with uniform density, we use a non-uniform mesh refined in the emitter region. Furthermore, we took advantage of the possibility offered by the FreeFem++ software to dynamically adapt meshes. In practice, we first compute a solution on a uniform mesh, generate an adapted mesh, project the solution onto the new mesh and relaunch Newton iteration (Cf [32]). As illustrated in figure B1, this procedure leads to the same precision but requires an order of magnitude less grid points. The resulting mesh is displayed in figure B2(a,b). Figure B2(c,d) illustrates the considered mesh, with an illustration on mesh refinement nearby the emitter. In most of the provided computations, more than 40 points grid points at the corona boundary Γ are reached by the iteration procedure so as to achieve the desirable precision. As exemplified in Figure B1 the total grid points N (better called degree of freedom number in FE) can be reduced to three thousand points when using successive adapted meshes.

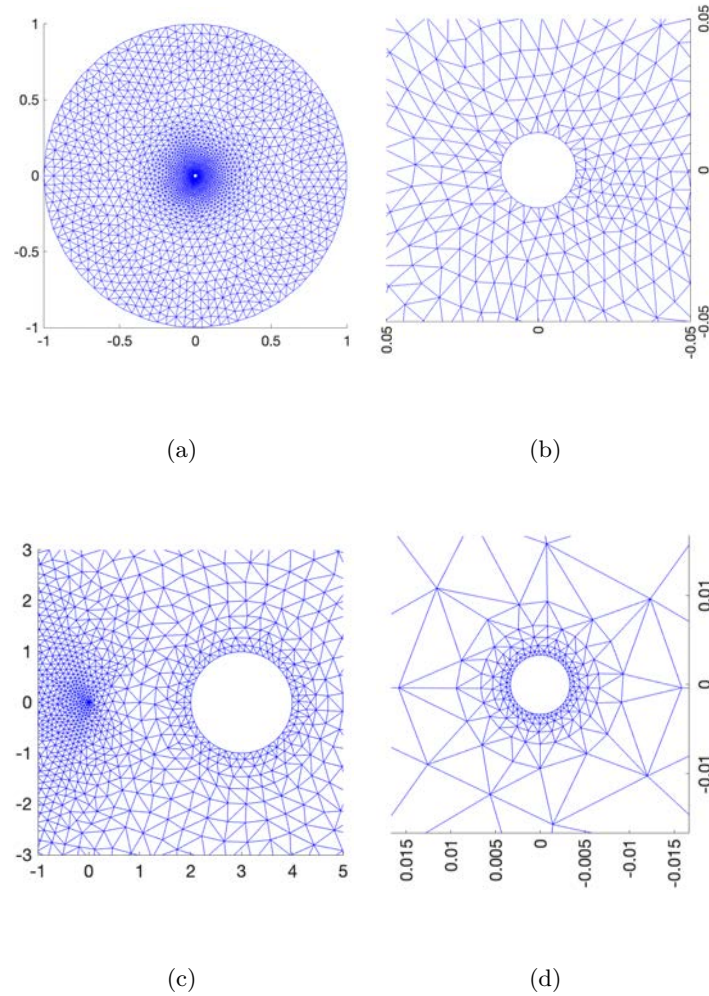


Figure B2: Illustration of the mesh refinement in various configurations. (a) & (b) For axi-symmetric configuration with $r_0/r_c = 0.0125$. (b) Zoom of Sub-figure (a) in the emitter's region. (c) & (d) For the 1E/1C configuration. (d) Zoom of Sub-figure (c) in the emitter's region.

Appendix C. Newton method

At each step of the Newton iteration method, the solution is searched as $[\hat{\varphi}, \hat{\rho}, \hat{\lambda}] \equiv [\hat{\varphi}^0, \hat{\rho}^0, \hat{\lambda}^0] + [\delta\hat{\varphi}, \delta\hat{\rho}, \delta\hat{\lambda}]$, where $[\hat{\varphi}^0, \hat{\rho}^0, \hat{\lambda}^0]$ is the approximate solution from the previous iteration and $[\delta\hat{\varphi}, \delta\hat{\rho}, \delta\hat{\lambda}]$ is the correction to approach the final solution. Injecting this ansatz in (25), (28) and (31) and linearizing in terms of the perturbations leads to the following linear system to be solved at each step:

This is the author's peer reviewed, accepted manuscript. However, the online version of record will be different from this version once it has been copyedited and typeset.
PLEASE CITE THIS ARTICLE AS DOI: 10.1063/5.0041061

$$\begin{aligned} \forall \varphi^\dagger, \quad & - \int_{\hat{\Omega}} \hat{\nabla} \delta \hat{\varphi} \cdot \hat{\nabla} \varphi^\dagger + \int_{\hat{\Omega}} \delta \hat{\rho} \varphi^\dagger + \frac{1}{\varepsilon_p} \int_{\partial \hat{\Omega}^c} \varphi^\dagger \delta \hat{\varphi} \\ & + \int_{\hat{\Gamma}} \varphi^\dagger \hat{E}_a - \int_{\hat{\Omega}} \hat{\nabla} \hat{\varphi}^0 \cdot \hat{\nabla} \varphi^\dagger + \int_{\hat{\Omega}} \hat{\rho}^0 \varphi^\dagger + \frac{1}{\varepsilon_p} \int_{\partial \hat{\Omega}^c} \varphi^\dagger \hat{\varphi}^0 = 0 \end{aligned} \quad (\text{C.1})$$

$$\begin{aligned} \forall \rho^\dagger, \quad & \int_{\hat{\Gamma}} \rho^\dagger \delta \lambda + \int_{\partial \hat{\Omega}^c} \rho^\dagger \left(\hat{\rho}^0 \hat{\nabla} \delta \hat{\varphi} + \delta \hat{\rho} \hat{\nabla} \hat{\varphi}^0 + \frac{\hat{\nabla} \delta \hat{\rho}}{Pe} \right) \cdot \mathbf{n} \\ & - \int_{\hat{\Omega}} \hat{\nabla} \rho^\dagger \cdot \left(\hat{n}^0 \hat{\nabla} \delta \hat{\varphi} + \delta \hat{\rho} \hat{\nabla} \hat{\varphi}^0 + \frac{\hat{\nabla} \delta \hat{\rho}}{Pe} \right) \\ & + \int_{\hat{\Gamma}} \rho^\dagger \lambda^0 \left(\hat{\rho}^0 \hat{\nabla} \hat{\varphi}^0 + \frac{\hat{\nabla} \hat{\rho}^0}{Pe} \right) \cdot \mathbf{n} - \int_{\hat{\Omega}} \hat{\nabla} \rho^\dagger \cdot \left(\hat{\rho}^0 \hat{\nabla} \hat{\varphi}^0 + \frac{\hat{\nabla} \hat{\rho}^0}{Pe} \right) = 0 \end{aligned} \quad (\text{C.2})$$

$$\begin{aligned} \forall \lambda^\dagger, \quad & \int_{\hat{\Gamma}} \lambda^\dagger \delta \hat{\varphi} + \varepsilon_\lambda \int_{\hat{\Gamma}} \frac{\partial \delta \lambda}{\partial s} \cdot \frac{\partial \lambda^\dagger}{\partial s} \\ & + \int_{\hat{\Gamma}} \lambda^\dagger (\hat{\varphi}^0 - 1) + \varepsilon_\lambda \int_{\hat{\Gamma}} \frac{\partial \lambda^0}{\partial s} \cdot \frac{\partial \lambda^\dagger}{\partial s} = 0 \end{aligned} \quad (\text{C.3})$$

- [1] Jack Wilson, Hugh Perkins, and William Thompson. An investigation of ionic wind propulsion. Technical report, NASA Report NASA/TM, 2009.
- [2] Kento Masuyama and S. R. H. Barrett. On the Performance of electrohydrodynamic propulsion. *Proc. R. Soc. A*, 50(6):1480–1486, 2013.
- [3] Konstantinos N. Kioulos, Antonios X. Moronis, and Wolf G. Fruh. Electro-Hydrodynamic (EHD) Thrust Analysis in Wire-Cylinder Electrode Arrangement. *Plasma Sci. Technol.*, 16(4):363–369, 2014.
- [4] Eric Moreau, Benard Nicolas, Lan-Sun-Luk Jean-Daniel, and Chabriat Jean-Pierre. Electrohydrodynamic force produced by a wire-to-cylinder dc corona discharge in air at atmospheric pressure. *J. Phys. D: Appl. Phys.*, 46(47):475204, 2013.
- [5] Christopher K. Gilmore and S. R. H. Barrett. Electrohydrodynamic thrust density using positive corona-induced ionic winds for in-atmosphere propulsion. *Proc. R. Soc. A*, 471(2175):20140912–20140912, 2015.
- [6] Christopher K Gilmore and Steven R H Barrett. Electroaerodynamic thruster performance as a function of altitude and flight speed. *AIAA. J.*, 56(3):1105–1117, 2017.
- [7] Nicolas Monrolin, Franck Plouraboué, and Olivier Praud. Electrohydrodynamic Thrust for In-Atmosphere Propulsion. *AIAA. J.*, 55(12):4296–4305, 2017.
- [8] Vladislav Yu Khomich and Igor E. Rebrov. In-atmosphere electrohydrodynamic propulsion aircraft with wireless supply onboard. *J. Electrostat.*, 95:1–12, 2018.
- [9] Haofeng Xu, Nicolas Gomez-Vega, Devansh R. Agrawal, and Steven R.H. Barrett. Higher thrust-to-power with large electrode gap spacing electroaerodynamic devices for aircraft propulsion. *J. Phys. D: Appl. Phys.*, 53(2), 2020.
- [10] Myron Robinson. Movement of air in the electric wind of the corona discharge. *T. Am. Inst. Elect. Eng.*, 80(2):143–150, 1961.
- [11] E.A. Christenson and P.S. Moller. Ion-Neutral Propulsion in Atmospheric Media. *AIAA. J.*, 5(10):1768–1773, 1967.
- [12] Eric Moreau and Gérard Touchard. Enhancing the mechanical efficiency of electric wind in corona discharges. *J. Electrostat.*, 66(1-2):39–44, 2008.
- [13] Haofeng Xu, Yiou He, Kieran L. Strobel, Christopher K. Gilmore, Sean P. Kelley, Cooper C. Hennick, Thomas Sebastian, Mark R. Woolston, David J. Perreault, and Steven R. H. Barrett. Flight of an aeroplane with solid-state propulsion. *Nature*, 563(7732):532+, 2018.
- [14] L Zhao and K Adamiak. Numerical analysis of forces in an electrostatic levitation unit. *J. Electrostat.*, 63(6-10):729–734, 2005.
- [15] Alexandre A. Martins and Mario J. Pinheiro. Modeling of an EHD corona flow in nitrogen gas using an asymmetric capacitor for propulsion. *J. Electrostat.*, 69(2):133–138, 2011.
- [16] Alexandre A. Martins and Mario J. Pinheiro. On the influence that the ground electrode

- diameter has in the propulsion efficiency of an asymmetric capacitor in nitrogen gas. *Physics of Plasmas*, 18(3):033512, 2011.
- [17] Davide Cagnoni, Francesco Agostini, Thomas Christen, Nicola Parolini, Ivica Stevanovic, and Carlo de Falco. Multiphysics simulation of corona discharge induced ionic wind. *J. Phys. D: Appl. Phys.*, 114(23):233301, 2013.
- [18] She Chen, Yifei Zhu, Jingyi Tu, and Feng Wang. Numerical investigation of an electroaerodynamic driven aeroplane: Electrical properties, ionic wind and flight performance. *J. Phys. D: Appl. Phys.*, 52(36), 2019.
- [19] Kazimierz Adamiak. Quasi-stationary modeling of the DBD plasma flow control around airfoil. Quasi-stationary modeling of the DBD plasma flow control around airfoil. *Phys. Fluids*, 085108, 2020.
- [20] Rakshit Tirumala and David B. Go. Comparative study of corona discharge simulation techniques for electrode configurations inducing non-uniform electric fields. *J. Electrostat.*, 72(2):99–106, 2014.
- [21] F Beux, A Iollo, MV Salvetti, and A Soldati. Approximation and reconstruction of the electrostatic field in wire-plate precipitators by a low-order model. *J. Comput. Phys.*, 170(2):893–916, 2001.
- [22] N.A. Kaptsov. *Elektricheskie Yavleniya v Gazakh i Vakuume*. Moscow, 1947.
- [23] Nicolas Monrolin, Olivier Praud, and Franck Plouraboué. Revisiting the positive DC corona discharge theory: Beyond Peek's and Townsend's law. *Phys. Plasmas*, 25:063503, 2018.
- [24] Yifei Guan, Ravi Sankar Vaddi, Alberto Aliseda, and Igor Novosselov. Analytical model of electro-hydrodynamic flow in corona discharge. *Phys. Plasmas*, 25(8):1–8, 2018.
- [25] Ravi Sankar Vaddi, Yifei Guan, Alexander Mamishev, and Igor Novosselov. Analytical model for electrohydrodynamic thrust. *Proc. R. Soc. A*, 476(2241), 2020.
- [26] Nuno Ferreira, Diego F Santos, Pedro G C Almeida, George V Naidis, and Mikhail S Benilov. Simulation of pre-breakdown discharges in high-pressure air i: The model and its application to corona inception. *J. Phys. D: Appl. Phys.*, 10.1088/1361-6463/ab2849, 2019.
- [27] Franck William Peek. *Dielectric phenomena in high voltage engineering*. McGraw-Hill Book Company, New-York, 1915.
- [28] Nicolas Monrolin, Olivier Praud, and Franck Plouraboué. Electrohydrodynamic ionic wind, force field, and ionic mobility in a positive dc wire-to-cylinders corona discharge in air. *Phys. Rev. Fluids*, 3(6):063701, 2018.
- [29] James Feng. An analysis of corona currents between two concentric cylindrical electrodes. *J. Electrostat.*, 46(1):37–48, 1999.
- [30] K. Yanallah, F. Pontiga, Y. Meslem, and a. Castellanos. An analytical approach to wire-to-cylinder corona discharge. *J. Electrostat.*, 70(4):374–383, 2012.
- [31] F. Hecht. New development in freefem++. *J. Numer. Math.*, 20(3-4):251–265, 2012.
- [32] D. Fabre, V. Citro, D. Ferreira Sabino, P. Bonnefis, J. Sierra, F. Giannetti, and M. Pigou. A Practical Review on Linear and Nonlinear Global Approaches to Flow Instabilities. *Applied Mechanics Reviews*, 70(6), 02 2019. 060802.
- [33] K. N. Kioussis, A. X. Moronis, and E. D. Fylladitakis. chapter Finite Element Analysis Method for Detection of the Corona Discharge Inception Voltage in a Wire-Cylinder Arrangement, pages 188–193. Number ISBN: 978-1-61804-184-5. 2013.
- [34] Yuesheng Zheng, Bo Zhang, and Jinliang He. Onset conditions for positive direct current corona discharges in air under the action of photoionization. *Phys. Plasmas*, 18(12), 2011.
- [35] G Horvath, J D Skalny, N J Mason, M Klas, M Zahoran, R Vladoiu, and M Manole. Corona discharge experiments in admixtures of N2 and CH4: a laboratory simulation of Titan's atmosphere. *Plasma Sources Sci. Technol.*, 18(12):1–7, 2009.
- [36] G. V. Naidis. Conditions for inception of positive corona discharges in air. *Journal of Physics D: Applied Physics*, 38(13):2211–2214, 2005.
- [37] A. A. Schnyder, R. Howling, D. Bommottet, and Ch. Hollenstein. Direct current breakdown in gases for complex geometries from high vacuum to atmospheric pressure. *J. Phys. D: Appl. Phys.*, 46:285205, 2013.